

## A NEW $z = 0$ METAGALACTIC UV BACKGROUND LIMIT\*

JOSHUA J. ADAMS

Department of Astronomy, University of Texas at Austin, 1 University Station, C1400, Austin, TX 78712

JUAN M. USON

Observatoire de Paris - LERMA, 61 Avenue de l'Observatoire, 75014 Paris, France

GARY J. HILL AND PHILLIP J. MACQUEEN

McDonald Observatory, University of Texas at Austin, 1 University Station, C1402, Austin, TX 78712

ACCEPTED TO APJ: December 13, 2010

### ABSTRACT

We present new integral-field spectroscopy in the outskirts of two nearby, edge-on, late-type galaxies to search for the  $H\alpha$  emission that is expected from the exposure of their hydrogen gas to the metagalactic ultraviolet background (UVB). Despite the sensitivity of the VIRUS-P spectrograph on the McDonald 2.7m telescope to low surface brightness emission and the large field-of-view, we do not detect  $H\alpha$  to  $5\sigma$  upper limits of  $6.4 \times 10^{-19}$  erg/s/cm<sup>2</sup>/□'' in UGC 7321 and of  $25 \times 10^{-19}$  erg/s/cm<sup>2</sup>/□'' in UGC 1281 in each of the hundreds of independent spatial elements (fibers). We fit gas distribution models from overlapping 21 cm data of HI, extrapolate one scale length beyond the HI data, and estimate predicted  $H\alpha$  surface brightness maps. We analyze three types of limits from the data with stacks formed from increasingly large spatial regions and compare to the model predictions: 1) single fibers, 2) convolution of the fiber grid with a Gaussian, circular kernel (10'' full width half maximum), and 3) the coadded spectra from a few hundred fibers over the brightest model regions. None of these methods produce a significant detection ( $> 5\sigma$ ) with the most stringent constraints on the HI photoionization rate of  $\Gamma(z = 0) < 1.7 \times 10^{-14}$  s<sup>-1</sup> in UGC 7321 and  $\Gamma(z = 0) < 14 \times 10^{-14}$  s<sup>-1</sup> in UGC 1281. The UGC 7321 limit is below previous measurement limits and also below current theoretical models. Restricting the analysis to the fibers bound by the HI data leads to a comparable limit; the limit is  $\Gamma(z = 0) < 2.3 \times 10^{-14}$  s<sup>-1</sup> in UGC 7321. We discuss how a low Lyman limit escape fraction in  $z \sim 0$  redshift star forming galaxies might explain this lower than predicted UVB strength and the prospects of deeper data to make a direct detection.

*Subject headings:* galaxies: evolution — diffuse radiation — intergalactic medium

### 1. INTRODUCTION

The strength of the metagalactic ultraviolet background (UVB) has great impact on theoretical models of structure formation (e.g. Haardt & Madau 1996) and a variety of physical processes such as the inhibition of small halo collapse (e.g. Efstathiou 1992), the intergalactic temperature and ionization state of the intergalactic medium (IGM) (e.g. Hui & Gnedin 1997), and IGM metallicity determinations (e.g. Rauch et al. 1997a). The likely contributors to the UVB are active galactic nuclei and star formation in galaxies (Schirber & Bullock 2003; Faucher-Giguère et al. 2008b) with appear compatible with observed populations (Gallego et al. 1995; Hopkins 2004; Hopkins et al. 2007; Bouwens et al. 2009) under reasonable corrections for dust attenuation, low luminosity extrapolations, redshift evolution, and escape fractions. The strength of the UVB, especially at low redshift (Davé & Tripp 2001), is still highly uncertain despite its importance. Most recent efforts have focused on high redshifts,  $z > 2$ , where the strongest UVB measurements exist. For instance, the detailed history of star formation (Madau et al. 1999; Faucher-Giguère et al. 2008a) and the potential to measure individual active galactic nuclei (AGN) host halo masses (Loeb & Eisenstein 1995; Faucher-Giguère et al. 2008c) have

been explored. Measurements of the photoionization rate have used three methods: observations of  $H\alpha$  such as described in this paper, the line-of-sight proximity effect method (e.g. Carswell et al. 1982; Bajtlik et al. 1988), and the flux decrement method (e.g. Cen et al. 1994; Rauch et al. 1997b). The latter two require backlighting quasars and are therefore difficult or impossible at low redshift. We are motivated to constrain the current model with a different, low redshift measurement. Instead of using Lyman- $\alpha$  forest features, we pursue a measurement of the UVB powered,  $H\alpha$  emission that should occur in the outskirts of local disk galaxies. As a secondary motivation, the kinematics of  $H\alpha$  at distances beyond HI data are important probes to the total dark halo masses in nearby disk galaxies (Christlein & Zaritsky 2008).

Galactic disks are optically thick to Lyman limit photons and maintain their observed HI distributions through self-shielding against the UVB. As recognized for decades (Sunyaev 1969; Felten & Bergeron 1969; Bochkarev & Sunyaev 1977), the influence of the UVB may be investigated in the extreme outskirts of disks where the self-shielding begins to fail. These early works sought to measure this effect through disk truncation in HI. However, there appear to be cases with (Corbelli et al. 1989; van Gorkom 1993) and without (Walsh et al. 1997; Carignan & Purton 1998; Oosterloo et al. 2007) HI truncations above the critical column density predicted using current UVB estimates, implying that other processes may strip gas and mimic the result.

Electronic address: jjadams@astro.as.utexas.edu

\* This paper includes data taken at The McDonald Observatory of The University of Texas at Austin.

Moreover, reaching the UVB implied truncation thresholds in 21 cm measured HI would require rather long observations with current facilities. A more robust signature of the UVB strength would be the detection of the H $\alpha$  in these outskirt regions. H $\alpha$  has been found at such radii before in actively star forming and warped galaxies by Bland-Hawthorn *et al.* (1997) (hereafter BFQ) with Fabry-Perot staring measurements. However, the  $\mu(H\alpha) = 2.3 \times 10^{-19}$  erg/s/cm<sup>2</sup>/□'' detection was interpreted to be due to non-UVB sources as indicated by an abnormally high [NII] $\lambda$ 6548 to H $\alpha$  ratio. Searches have also yielded limits in quiescent systems (Vogel *et al.* 1995; Weymann *et al.* 2001; Madsen *et al.* 2001) with an upper limit for the UVB photoionization rate,  $\Gamma$ , of  $\Gamma(z = 0) < 2.4 - 9.5 \times 10^{-14} \text{s}^{-1} (2\sigma)$  being the deepest. The wide range due on this limit is due to gas cloud geometrical uncertainty. Despite the numerous theoretical implications and the efforts of numerous groups, a UVB powered H $\alpha$  detection still awaits discovery.

The tactical advantages we bring to this problem are deep surface brightness limits, a large two dimensional field of view through integral field spectroscopy compared to the previous longslit and Fabry-Perot staring data, and target selection of very high inclinations to maximize signal and minimize contamination uncertainty. Our targets are edge-on, low surface brightness Sd galaxies that are rather isolated and minimally warped in order to avoid density distribution uncertainties and exposure to internally generated ionization from smaller radii. Indeed, our most constraining target, UGC 7321, has a gas surface density below that required for significant star formation (Kennicutt 1989) at all radii, as well as being unusually isolated with no known companions and minimal ( $< 3^\circ$ ) warping (Uson & Matthews 2003).

In this paper we begin with a description of the simple ionization state and density model of disk galaxies that will be used to link a measured H $\alpha$  surface brightness with a particular UVB photoionization rate in §2.1. In §2.2, we give disk parameter constraints based on fits to existing 21 cm data. In §2.3, we argue that UGC 7321 in particular is likely to extend its HI profile beyond the current 21 cm limits without truncation. In addition, the HI observations of UGC 7321 are amongst the most sensitive such measurements published to-date. The 21 cm data allow a very precise model to be made for the gas distribution in the galaxy outskirts at the locations where we search for H $\alpha$  emission. Next, in §3, we present deep integral field spectroscopy observations at radii corresponding to the outermost detections of 21 cm emission and beyond. We describe the choices made to stack spectra at various spatial scales. The stacked spectra are searched for H $\alpha$  detections and upper limits are derived. Particular focus is given to systematic errors. Finally, in §4, we discuss the context, the likely cause of the unexpectedly low limit, and further observations that can confirm our conclusions. The Appendix A provides the analytic details necessary to construct the full and general H $\alpha$  surface brightness distribution model. We will quote most of the surface brightness limits in units of erg s<sup>-1</sup> cm<sup>-2</sup> arcsec<sup>-2</sup>, but for easy comparison to alternative units we note the conversion at the wavelength of H $\alpha$  of 1 millirayleigh (mR) =  $5.66 \times 10^{-21}$  erg s<sup>-1</sup> cm<sup>-2</sup> arcsec<sup>-2</sup> =  $2.8 \times 10^{-3}$  cm<sup>-6</sup> pc in emission measure assuming the case B coefficient we adopt.

## 2. HI BASED MODELS AND H $\alpha$ PREDICTIONS

### 2.1. Model assumptions

A three dimensional gas density distribution must be inferred in order to translate H $\alpha$  surface brightness into a UVB strength. BFQ made estimates assuming exponential forms both radially and vertically in the gas distribution with a plane parallel assumption. Motivated by the regular HI structure on local scales (García-Ruiz *et al.* 2002; Uson & Matthews 2003) of our chosen targets showing simple exponential trends and needing an extrapolated model in gas density for interpretation of UVB limits, we also assume exponential forms.

In order to interpret H $\alpha$  measurements generically inside and outside of the UVB photoionization front around gaseous disks, we have generalized the model of BFQ. Some toy calculations in the model also show the importance of high inclination selection to make the deepest possible UVB constraints. This high inclination boon has been known before, but not carefully followed in earlier works' target selection. The model assumes both regular gas distributions and sharp photoionization transitions in a plane parallel approximation under arbitrary disk inclinations and sight lines. Our model assumes sharp photoionization fronts exist. We verify this assumption by estimating the Lyman limit photon mean free path at the midplane ionization front. In their Equation 3, BFQ estimate the hydrogen density at this point as  $n_H \approx 0.05 \text{cm}^{-3}$ . The Lyman limit photon mean free path is given by  $l_{mpf} \approx (n \times a_\nu)^{-1} \approx 1.1 \text{pc}$  with  $a_\nu$  (Osterbrock & Ferland 2006) as the hydrogen Lyman limit photoionization cross section. This is much smaller than the common disk scale lengths in either direction. The vertical scales for cold disk galaxies are of order 100 pc or greater. More sophisticated models can be made (Maloney 1993; Dove & Shull 1994) by solving for the ionization and excitation states of hydrogen and helium with full radiative transfer solutions in a grid of plane-parallel gas layers, but such an analysis is beyond the scope of this work.

The forthcoming derivation follows BFQ equations 1-6. The important differences are that this derivation is generalized for any viewing inclination,  $i$ , and for arbitrary positioning of the spectral data in the galaxy's field of observation. The BFQ derivations were specifically for  $i = 0^\circ$  and the field position along the major axis where all gas is photoionized. We denote the generic surface brightness in H $\alpha$  as  $\mu$ . We denote  $\mu_0$  as the special case of the peak H $\alpha$  surface brightness where the photoionization front intersects the disk midplane. Our results reduce to the BFQ values of  $\mu_0$  for  $i = 0^\circ$ . In Equation 1 we give the assumed gas distribution in cylindrical coordinates  $R$  and  $z$  with radial scale-length  $h_r$ , vertical scale length  $h_z$ , and central hydrogen density  $n_0$ .

$$n_H(R, z) = n_0 \exp\left(\frac{-|z|}{h_z}\right) \exp\left(\frac{-R}{h_r}\right) \quad (1)$$

The commonly assumed form of the UVB spectrum is given in Equation 2 where  $\nu$  is the frequency,  $\nu_0$  is the Lyman limit frequency,  $J_0$  is the UVB strength at the Lyman limit in units of erg cm<sup>-2</sup> s<sup>-1</sup> Hz<sup>-1</sup> sr<sup>-1</sup>, and  $\beta$  is the UVB spectral index.

$$J_\nu = J_0 \left(\frac{\nu_0}{\nu}\right)^\beta \quad (2)$$

Another common form of quoting the UVB strength is with the UVB photoionization rate,  $\Gamma$ . We show this form in Equation 3 where  $h$  is Planck's constant,  $\sigma(\nu)$  is the hydrogen photoionization cross section, and  $a_\nu = \sigma(\nu_0)$  is the Lyman limit cross section. The final equality in Equation 3 comes from the

standard power law approximation to the cross section shape (Osterbrock & Ferland 2006).

$$\Gamma = 4\pi \int_{\nu_0}^{\infty} \frac{J_{\nu}\sigma(\nu)}{h\nu} d\nu = \frac{4\pi a_{\nu} J_0}{h \times (3 + \beta)} \quad (3)$$

In Equation 4 we equate recombination and ionization rates under a plane parallel approximation. For the radial regions where any self-shielding can take place, we consider the top and bottom of the disk to each see incident flux from only half their total solid angle. We define  $n_e$  as the electron density,  $n_p$  as the proton density,  $\xi$  as the ionization fraction,  $\alpha_B$  as the case B recombination coefficient, and  $z_c(R)$  as the height above the midplane to which the photoionization front penetrates at radius  $R$ . We define  $\varepsilon$  as the volume filling factor, assumed to be spatially invariant. A clumpy gas distribution can, to first order, be represented by using this term somewhat lower than the nominal value of unity. With the assumption of sharp ionization boundaries, we can equate the gas densities as  $n_e = n_p = \xi n_H$  at radii beyond the photoionization front.

$$\alpha_B \int_{z_c(R)}^{\infty} \xi^2 \varepsilon n_H^2(R, z) dz = \int_{\nu_0}^{\infty} \frac{2\pi J_{\nu}}{h\nu} d\nu = \frac{2\pi J_0}{h\beta} \quad (4)$$

We next define a threshold radius,  $r_c$ , to which the UVB penetrates fully through the disk plane, so  $z_c(r_c) = 0$ . The solution of Equation 4 leads to Equations 5 and 6.

$$r_c = (\ln(2\xi^2 \varepsilon \alpha_B a_{\nu} n_0^2 h_z \beta) - \ln(\Gamma \times (3 + \beta))) \times h_r / 2 \quad (5)$$

$$z_c(R) = \begin{cases} \pm(r_c - R) \times h_z / h_r & : R \leq r_c \\ 0 & : R > r_c \end{cases} \quad (6)$$

Next, we define the variable  $\rho$  as the distance from the disk's midplane along the line-of-sight, spanning  $-\infty$  to the observer and  $\infty$  away from the observer. We also define the major axis position  $b_1$ , and minor axis position  $b_2$  as the observed field positions projected onto the sky. Finally, we represent the galaxy's inclination with  $i$ . Simple transformations to cylindrical coordinates give the expressions in Equations 7 and 8.

$$|z| = \sqrt{\rho^2 \cos^2 i + b_2^2 \sin^2 i + 2\rho b_2 \sin i \cos i} \quad (7)$$

$$R = \sqrt{\rho^2 \sin^2 i + b_2^2 \cos^2 i + b_1^2 - 2\rho b_2 \sin i \cos i} \quad (8)$$

The H $\alpha$  surface brightness,  $\mu(b_1, b_2)$ , follows directly from a line-of-sight integration. The full evaluation of  $\mu(b_1, b_2)$  involves finding the values of  $\rho$  that intersect the photoionization surface described by  $z_c(R)$  with field positions  $b_1$  and  $b_2$ . The analytic solutions to those intersections are given in Appendix A. The solution for the special case at field position  $b_2 = 0$  and  $b_1 = r_c$  gives the aforementioned peak surface brightness  $\mu_0$ , which is itself a useful measurement parameter, as related in Equation 9. In Equation 9,  $\gamma$  is the generally non-analytic integration of the emissivity along the line of sight,  $\alpha_{H\alpha}^{\text{eff}}$  is the case B effective H $\alpha$  recombination coefficient, and  $\Omega$  is the full sky solid angle of  $4\pi$  sr. For the gas density parameters we derive in our target galaxies in §2.2 and the areas we observe in §3, the face-on column densities of total hydrogen are sufficient ( $> 10^{17} \text{ cm}^{-2}$ ) to be everywhere optically thick to Lyman limit photons, let alone Lyman- $\beta$  and the other important lower energy transitions.

We use  $\alpha_{H\alpha}^{\text{eff}} = 1.17 \times 10^{-13} \text{ cm}^3 \text{ s}^{-1}$  as appropriate for  $T = 10^4 \text{ K}$  (Osterbrock & Ferland 2006).

$$\mu_0 = \frac{2h\nu_{H\alpha} \alpha_{H\alpha}^{\text{eff}} \int_0^{\infty} n_e(R, z) n_p(R, z) d\rho}{\Omega} = \frac{2\xi^2 \varepsilon \alpha_{H\alpha}^{\text{eff}} n_0^2 h\nu_{H\alpha} \gamma}{\Omega} \quad \text{with } \gamma = \int_0^{\infty} \exp\left(-\frac{2\rho \cos i}{h_z} - \frac{2\sqrt{r_c^2 + \rho^2 \sin^2 i}}{h_r}\right) d\rho \quad (9)$$

We explain the use of certain constants and assumed values to Equation 9. The ionization fraction is assumed to be unity by the earlier discussion of the Lyman limit mean free path. The volume filling factor may approach unity as there is no indication of star formation at extended scales in these galaxies. We will discuss the evidence for the absence of extended star formation in Section 4. Furthermore, the deprojection of the HI distribution in Uson & Matthews (2003) gives a peak surface density of only  $5.8 M_{\odot} \text{ pc}^{-2}$  at the center of UGC 7321. The surface density drops by over an order of magnitude at the locations we observe. These surface densities are well below the dynamical criterion for efficient star formation (Kennicutt 1989) and make a smooth gas distribution plausible. It is not possible to exclude small scale clumpiness, so we retain the volume filling factor. The case B and H $\alpha$  effective recombination coefficients are dependent on electron temperature. Following Weymann et al. (2001) and the discussion therein, we adopt  $T=10,000 \text{ K}$  and the values of Osterbrock & Ferland (2006). The true electron temperature may plausibly be different by a factor of two, leading to corresponding changes in  $\alpha_{H\alpha}^{\text{eff}}$  and  $\alpha_B$  of the same order of magnitude. However, the linearization in  $\Gamma$  of Equation 9 makes the surface brightness depend on the ratio of these two recombination coefficients, so their similar behavior with electron temperature cancels. For consistency with previous works, we do not propagate the recombination coefficient uncertainties as systematics to the final UVB limit.

Some brief numerical examples set the expected orders of magnitude, quantify the achievable limits under different galaxy geometries, and illustrate the important parameter dependencies under linear expansions. We look at some trial cases with  $\varepsilon = 1$ ,  $h_r = 1000 \text{ pc}$ ,  $h_z = 100 \text{ pc}$ ,  $\beta = 1.8$ ,  $\Gamma = 4 \times 10^{-14} \text{ s}^{-1}$ , and  $n_0 = 5 \text{ cm}^{-3}$ . For  $i = 0^\circ$ ,  $\gamma = \exp(-2r_c/h_r) \times h_z/2$  so  $\mu \approx 3.0 \times 10^{-20} \text{ erg/s/cm}^2/\square''$ . For  $i = 90^\circ$ ,  $\gamma = r_c K_1(2r_c/h_r)$ .  $K_1(x)$  is the modified Bessel function. In this case,  $\mu \approx 1.3 \times 10^{-18} \text{ erg/s/cm}^2/\square''$ . For this work's applications, the surface brightness profiles are smoothed by seeing and sampled by large fibers. Realistic smoothing and sampling, of order several arcseconds, can lower these peak values by several tens of percent. We will assume for all calculations that  $\beta = 1.8$  as motivated by previous models (Shull et al. 1999) and to aid the comparison with previous observational work that used the same assumption (Weymann et al. 2001). We note that  $\mu_0$  scales exactly linearly with  $\Gamma$  when viewed face-on and nearly linearly for all other inclinations. This is easily demonstrated by taking the large argument asymptotic behavior of the modified Bessel function which yields a linear scaling in  $\Gamma$  after a first order expansion. We show the small error caused by assuming a linear relation between  $\mu_0$  and  $\Gamma$  in Figure

1 for reasonable geometries. All further estimations of  $\Gamma$  in this work will be made in the linear approximation. We have linearized our estimate around  $\Gamma = 4 \times 10^{-14} \text{ s}^{-1}$  because we consider it the best current estimation from the work of Faucher-Giguère *et al.* (2009). However, any initial value would have worked as the only effect of a particular choice is that the small non-linearities pivot around the simulation UVB choice, but this error is negligible compared to our other error terms. The discussed numerical example between  $i = 0^\circ$  and  $i = 90^\circ$  also shows how the selection of thin, edge-on disks can exploit a particular flux limit to a  $(30 - 50\times)$  stronger UVB constraint than for face-on disks. We also emphasize with Equation 9 that the first order effects near  $i=90^\circ$  on distance, volume filling factor, and gas density cancel out;  $\mu_0$  only has first order dependence on  $i$ , the ratio of scale lengths,  $\frac{3+\beta}{\beta}$ , and  $\Gamma$ .

## 2.2. HI data

Three-dimensional gas distributions must be inferred for individual galaxies to interpret  $H\alpha$  surface brightness and to guide the stacking choices amongst fibers. We will use such fits to extrapolate the density profiles to larger radii where the  $H\alpha$  emission is predicted to reach peak surface brightness. The parameters from stellar distributions could potentially be used, but 21 cm measured HI is the more relevant indicator to ionized hydrogen. We adopt distances of 10 Mpc for UGC 7321 (Uson & Matthews 2003) and 5 Mpc for UGC 1281 (Tully *et al.* 2006). Low redshift surface brightness is insensitive to distance, so the exact distances are unimportant to this work. Different literature estimations have 50% and 10% rms ranges for the UGC 7321 and UGC 1281 distances respectively. We indicate scale lengths by the terms  $d_{10}$  as the actual distance to UGC 7321 in units of 10 Mpc and  $d_5$  as the actual distance to UGC 1281 in units of 5 Mpc. For reference, the scale conversions become  $48.5d_{10} \text{ pc}''$  for UGC 7321 and  $24.2d_5 \text{ pc}''$  for UGC 1281.

UGC 7321 was observed by one of us in collaboration with L. D. Matthews (Uson & Matthews 2003) using the second most-compact (C) configuration of the VLA<sup>2</sup> which includes some of the shortest spacings available and their full coverage, deep observations yielded spacings down to 28m, close to the dish diameter. Their quasi-naturally weighted (“robust” parameter  $\mathcal{R} = +1$ ) images recovered the full single-dish flux and, moreover, their single-dish equivalent spectrum matched the features of the best single-dish spectrum to within the (higher) uncertainty of the single-dish observations (Uson & Matthews (2003), fig. 6). For this paper, we have used their quasi-uniformly ( $\mathcal{R} = -1$ ) weighted images because of their better resolution ( $\sim 12''$ ) although the somewhat higher (45%) noise level only recovers  $\sim 96\%$  of the total flux. However, the five parameter model fits to the zeroth moment maps, described below, recover some of the lost flux and the remaining uncertainties only slightly shift the position of the predicted  $H\alpha$  peak.

For UGC 1281, we have reduced the raw data from the VLA archive. It was observed under proposal AZ097 on 1997 December 26 in the most compact (D) configuration for a total of 3 hours on source with interspersed observations of the strong, primary calibrator J0137+3309 (3C48) for which we have adopted the VLA recommended flux density

of 15.9 Jy. The observations were spaced over a range of  $\pm 3$  hours in H.A. giving excellent uv-coverage and images with 127 channels of width  $\sim 2.6 \text{ km s}^{-1}$  after standard on-line Hanning-smoothing. The angular scale that corresponds to the shortest baseline ( $\sim 900''$ ) is sufficiently larger than the largest single-channel galaxy extent ( $\sim 285''$ ) that the array should have recovered the total HI flux. We followed the same reduction steps as for UGC 7321 (Uson & Matthews 2003) to obtain a “cube” of spectral images using nearly-natural weighting ( $\mathcal{R} = +1$ ) which gave images with resolution  $\sim 51''$  which were free of artifacts to the rms sensitivity  $\sigma \sim 1.0 \text{ mJy/beam}$  per channel. We computed moment maps after applying a standard “ $1-\sigma$  cutoff” evaluated on a cube Gaussian-smoothed spatially to  $70''$  and Hanning-smoothed in frequency which led to a total HI flux of  $41 \pm 2 \text{ Jy km s}^{-1}$  corresponding to a mass of  $2.3 \times 10^8 d_5^2 M_\odot$ . The total flux is in good agreement with the values in the literature which range from (35.8 to 38.9) Jy km/s from two different single-dish measurements (Huchtmeier 1989) with the spread and uncertainty due in part to some ringing from strong in-band HI emission from the Milky Way as well as to calibration uncertainties. Again, we have obtained a spectral “cube” with nearly-uniform weighting ( $\mathcal{R} = -1$ ) which gave images with resolution of  $\sim 42''$  with rms sensitivity  $\sigma \sim 1.5 \text{ mJy/beam}$  per channel. As in UGC 7321, the higher noise level results in a slightly lower total flux,  $39 \pm 2 \text{ Jy km s}^{-1}$ .

Next, we characterize the HI distributions nearest our  $H\alpha$  observations. We have derived five parameter fits in  $n_0, h_r, h_z, i$ , and position angle to the zeroth moment maps of UGC 7321 and UGC 1281 through non-linear least squares minimization. The models include convolution to the instrumental beams of  $\sim 12''$  and  $\sim 42''$  FWHM and sampling of  $H\alpha$  appropriate to the fiber data. Both the maps show at least two major axis power law slopes, as Christlein *et al.* (2010) have found to be common in extended gaseous disk gas. We do not try to model the full gas distributions, but only the large radius trends by restricting the fits heavily to the outermost data regions. Still, the model fits deviate from the data by an amount that exceeds the observational errors. Some minor warps and substructure are visible. The formal errors in the total line intensity images are  $15 \times 10^{18} \text{ cm}^{-2}$  for UGC 7321 and  $5 \times 10^{18} \text{ cm}^{-2}$  for UGC 1281, which are both far smaller than the residuals to the best fit models. In order to capture the systematic model errors, we have made Monte Carlo simulations between the data and the best fit models to create 68% confidence intervals as given in Table 1 for all disk parameters and  $H\alpha$  observables. The perturbations in the Monte Carlo simulations are made from the residuals of the best fit model, not the statistical errors, to include the influence of systematics. These simulations allow us to create three types of  $H\alpha$  surface brightness prediction, with different scales of spatial co-addition, under an assumed  $\Gamma$ . Note that many of the individual disk parameters in Table 1 have large relative uncertainties, but the surface brightness predictions have small relative uncertainties. The disk parameters share degeneracies, as captured in the Monte Carlo simulations, that create highly certain  $H\alpha$  predictions despite the individually uncertain gas parameters. Predictions can be made for individual fibers, but to both mitigate the model uncertainties and improve our limits, we include predictions with a  $10'' \times 10''$  FWHM convolution sampled near the peak surface brightness positions. The exact choice of kernel size is not important, but is chosen to combine several neighboring fibers. Finally, we include a prediction for the average surface brightness of

<sup>2</sup> The Very Large Array of the National Radio Astronomy Observatory is a facility of the National Science Foundation, operated under cooperative agreement by Associated Universities, Inc.

all fibers expected to sample  $\mu > 10^{-19}$  erg/s/cm $^2$ /□". These various predictions will be compared to co-added data in §3. We give in Figure 2 the HI fits along major and minor axis cuts. The fits to UGC 7321 use all the HI data beyond an inner radius cut, which was chosen to avoid a substructure bump near  $R \approx 140''$ . The fits to UGC 1281 are more constrained with both an inner and outer radius cut. The outer cut is to exclude a known  $\sim 8^\circ$  warp (García-Ruiz et al. 2002). The fitting function assumes a single position angle at all radii and does not describe warps well. We have investigated the disk's outer behavior by also deriving fits from the  $R > 220''$  data alone. A radial scale length compatible with, but noisier than, the Table 1 value was found with a significant change in position angle, a reflection of the warp.

### 2.3. HI bounded limit

While we cannot definitively prove that these galaxies maintain their extrapolated hydrogen profiles over the galactocentric distances we will discuss in §2.2, such an assumption is reasonable with the current 21 cm data. There is no evidence for flaring in these galaxies, and the superthin shape implies an undisturbed history. In UGC 7321, Uson & Matthews (2003) have searched for low-mass companions and found none to the limit of  $M_{HI} = 2.2 \times 10^6 M_\odot$  within  $12'(35$  kpc). The nearest optical companions are two dwarf galaxies at minimum distances of 340 kpc, implying minimum times to last encounter of  $1.6 \times 10^9$  years. So, it is unlikely that gas has been stripped from the regions over which we have extrapolated a density profile. However, we have calculated an alternative limit using data bounded by the HI data in a manner similar to the analysis in Stocke et al. (1991); Vogel et al. (1995); Donahue et al. (1995); Weymann et al. (2001) as an alternative, which is equivalent to assuming that the gas is completely truncated where the 21 cm signal falls below the noise. In those works, a single, simple equation based on global photoionization equilibrium is used and here repeated in Equation 10.

$$\Phi = \Gamma \frac{3 + \beta}{4a_\nu \beta} = \frac{I_{H\alpha}}{f_a f_{H\alpha}} \frac{A_{proj}}{A_{tot}} \quad (10)$$

The variable  $\Phi$  is the one-sided incident ionizing UVB flux in units of cm $^{-2}$  s $^{-1}$ ,  $I_{H\alpha}$  is the H $\alpha$  surface brightness in units of  $\mu R$ ,  $f_a$  is the fraction of incident photons that become absorbed when passing through the face-on cloud,  $f_{H\alpha}$  is the fraction of excited recombinations that produce an H $\alpha$  photon,  $A_{proj}$  is the projected area covered by spectroscopy and 21cm data, and  $A_{tot}$  is the total surface area for the regions in projection that can absorb Lyman limit photons. The area aspect ratio is usually determined from 21cm data. This calculation takes no account of the spatial stratification between 21cm and H $\alpha$  that can realistically occur for very thin gas distributions, as we will see later in §2.2 where the predicted H $\alpha$  surface brightness is derived, and requires H $\alpha$  searches and interpretations to be restricted to area covered by deep 21cm data. However, for mild aspect ratios ( $\sim < 10$ ) or large 21cm beams, this method delivers similar predictions as those in §2.1.

We now discuss the evaluation of the few terms in this model. The assumption in the HI bounded limit is that the hydrogen resides within some well-defined area represented by the noise floor of the 21cm data. It is not obvious how the area should be defined in a continuous gas distribution, but we adopt the photoionization front we have previously defined in

Equations 5 and 6 as a realistic edge. In §2.2 we determine gas geometries for our target galaxies. In particular for the area in UGC 7321 covered by fibers, with  $N_{HI} > 10^{19}$  cm $^{-2}$ , and the parameters in Table 1, we find  $\langle \frac{A_{tot}}{A_{proj}} \rangle = 24.8_{-1.5}^{+3.4}$ . This value is in good agreement with the 21cm axis ratio of 29 determined at the  $10^{20}$  cm $^{-2}$  contour in Uson & Matthews (2003, Table 3). By adopting this distribution in face-on column density and a UVB spectral index of  $\beta = 1.8$ , we can evaluate  $f_a$ . We find  $\langle \frac{A_{tot} f_a}{A_{proj}} \rangle = 22.8_{-1.8}^{+4.4}$  in UGC 7321. With the same calculations applied to UGC 1281, we find  $\langle \frac{A_{tot}}{A_{proj}} \rangle = 19.0_{-1.8}^{+5.6}$  and  $\langle \frac{A_{tot} f_a}{A_{proj}} \rangle = 13.6_{-2.0}^{+6.2}$ . Identically to Weymann et al. (2001), we adopt  $f_{H\alpha} = 0.45$  as appropriate for case B and a  $10^4$ K electron temperature. We also carry out this analysis in Tables 1 and 2 for continuity with previous work, but we emphasize that our preferred limit comes from the comparisons to the model in §2.1 as it incorporates the spatial segregation between the brightest H $\alpha$  regions and the HI data that is natural in very thin, edge-on geometries.

## 3. H $\alpha$ DATA AND ANALYSIS

We have obtained new integral field spectroscopy positioned along the major axes of UGC 7321 and UGC 1281 targeting H $\alpha$  with the Visible Integral-field Replicable Unit Spectrograph Prototype (VIRUS-P, Hill et al. 2008) on the McDonald 2.7m telescope. We observed UGC 1281 on 2009 October 22-24 with  $R = 1288$  from 4700-6990Å for 21 photometric hours and UGC 7321 on 2010 April 9 and 11 with a resolution of  $R = 3860$  from 6040-6740Å for 15 hours under non-photometric conditions. Between the  $R = 1288$  and  $R = 3860$  observations, made possible by a new grating, we not only gain in sensitivity scaled by the square root of the resolution but resolve the bright skylines, OH  $\lambda 6568.779$  and geocoronal H $\alpha$ , from our target wavelengths. We have set the controller to bin pixels by two in the wavelength direction which samples the spectra just at the Nyquist criterion and minimizes read noise. The VIRUS-P field covers a  $1'6 \times 1'6$  field with 246 fibers of  $2''05$  radius with a one-third fill-factor. We split our observations into three dithers to cover the entire field. In UGC 1281 we split our time further between two overlapping fields to cover the outer plane better in the presence of a possible  $< 8^\circ$  warp (García-Ruiz et al. 2002) yielding a total of six dithers. Spectrophotometric flux standard stars from Massey et al. (1988) were measured once or twice nightly. We tracked the transparency through the offset guiding camera. Galactic extinction corrections (Schlegel et al. 1998; O'Donnell 1994) were made with  $A_V = 0.09$  and  $A_V = 0.15$  for UGC 7321 and UGC 1281 respectively. A spectral airmass/extinction curve specifically modelled for the McDonald Observatory site was applied. We estimate its systematic uncertainty by comparing it to the Kitt Peak curve supplied with the IRAF package onedspec. We find a 20% rms difference between the wavelengths of 6000-7000Å. The two curves deviate systematically at  $\lambda > 5900$ Å. We believe the site specific McDonald curve to be more accurate to our data. However, we propagate the difference as a potential, systematic uncertainty. The flux calibration uncertainty due to the airmass/extinction curve at the data's median airmass of 1.09 is  $\pm 0.023$  magnitudes.

### 3.1. Flux calibration

The  $8'$  offset guiding camera is an Apogee Alta with a  $20.25 \square'$  field-of-view under a B+V ( $\lambda_{\text{mean}} = 5000$ Å) filter.

Guider images were read out and saved every few seconds. Stacks of guider images that overlapped in time with each individual VIRUS-P exposure (20 minutes each on UGC 1281, 30 minutes each on UGC 7321, and 1 minute each on the flux standards) were combined. We make a relative photometry correction to each science frame based on the stack of guider images taken simultaneously with the VIRUS-P data. Typically, ten stars per guider frame were available for photometry.

We have switched from the standard stars to the science targets with gaps of less than 5 minutes and assumed the conditions to be constant over that time and between the standard star and galaxy positions to make the absolute flux calibration. The observations of standard stars were taken during the most photometrically stable periods during each night to mitigate this potential source of error. Even so, the final flux calibration factor we apply may have systematic errors. We assess this error by considering the 5 observations of 2 standards, PG1708+602 and Feige 34, taken along with the UGC 7321 data and the 3 observations of 1 standard, Feige 110, taken along with the UGC 1281 data. The distribution in flux calibrations is wavelength-independent over our observed range with a 6.8% rms and 2.2% rms respectively. These estimates also capture possible variation in transparency with on-sky position. They are reported in Table 2 along with the possible error in the extinction curve between the effective wavelength of the guider and the wavelength of  $H\alpha$ . For the non-photometric data on UGC 7321, we measured a median zero-point change,  $\Delta z_p$ , of 0.276 magnitudes and a 68% range of 0.171-0.382 magnitudes over the two nights. The more nearly photometric data on UGC 1281 had median  $\Delta z_p = 0.057$  magnitudes and a 68% range of 0.043-0.077 magnitudes over the three nights.

### 3.2. Sky background subtraction

The choice of sky subtraction is particularly important for this work which reaches for flux limits far below the average sky brightness. If the science field were covered with source emission, sky nods would be necessary. Then, the time variability of the OH and geocoronal  $H\alpha$  sky lines would form important systematic error sources. Fortunately, the large VIRUS-P field of view and selection of extremely thin, edge-on target galaxies affords a subset of fibers that contain a negligible amount of source flux to serve as simultaneously measured sky fibers. We selected fibers sufficiently far from the major axis such that the models predicted  $\mu < 2 \times 10^{-21}$  erg/s/cm<sup>2</sup>/□'' (with the baseline  $\Gamma = 4 \times 10^{-14}$  s<sup>-1</sup>), or 100× below the expected peak surface brightness, to be used for sky subtraction. This cut left 24% and 44% of the fibers for sky estimation in UGC 7321 and UGC 1281 respectively. We experimented with moving this sky fiber cut up and down by a factor of five and found no difference in the final upper limits to the UVB strength. Depending on the number of fibers co-added, the statistical  $H\alpha$  flux errors presented here reach to 300× dimmer than the sky level. Without simultaneously measured sky background, the systematics of sky nods would quickly dominate the limits.

### 3.3. Data reduction

The data reduction, optimal background subtraction, and search for emission lines were completed with algorithms developed for a Lyman- $\alpha$  emitter survey (Adams *et al.* 2010). We summarize here the important steps. First, overscans and a

master bias frame are subtracted from each frame. The wavelength solution for each fiber is fit as a fourth order polynomial to  $\sim 30$  emission lines from HgCd lamps passing through the entire telescope light path. The residuals to the solution are of order one hundredth of a resolution element. Flat fields precise to  $< 1\%$  are made from twilight flats with the solar spectrum removed by a b-spline fit (Dierckx 1993) and division. This fit method is the same as we apply to fitting and subtracting the sky background and has important advantages over data interpolation. By avoiding data resampling, we keep the errors largely uncorrelated. Small distortions of the instrument camera over a regular pixel grid lead to the spectrum from each fiber being sampled at slightly different wavelengths. By considering a collection of fibers together in a fit, the spectrum is oversampled, and we can recover nearly blended features. This method delivers an optimal spectral model robust against cosmic rays and without the residuals that linear interpolation can create. A thorough description of b-spline fits as applied to astronomy datasets can be found in Kelson (2003). The next step in the data reduction is to fit and subtract a b-spline sky background modelled from selected sky fibers. Next, cosmic rays are masked by finding all pixels that deviate from the other pixels in the same fiber by some large threshold value. Some dim cosmic rays are missed by this step, but are rejected when combining multiple frames. We have chosen a threshold that misses the weakest  $\sim 20\%$  of cosmic rays for direct masking in this work. The exact threshold does not affect the results. The frame is then flux calibrated with the non-photometric zeropoint correction and airmass correction applied. Finally, a one dimensional final spectrum for each fiber position is created by combining all the frames taken at the same dither position and running across the 5 pixel cross-dispersion aperture. For the final estimate to be immune to remaining cosmic rays we have used the biweight estimator (Beers *et al.* 1990) at this step. Our pipeline makes no cross-talk correction since we restrict our cross-dispersion apertures to 5 pixels where the fiber separations are typically 8 pixels and the cross-dispersion FWHMs are typically 4 pixels. This leads to, at most, 10% contamination from neighboring fibers and becomes especially trivial when considering large collections of fibers as an aperture. The scattered light properties of the instrument have been characterized in Adams *et al.* (2008) and, particularly at  $H\alpha$  wavelengths, no scattered light or ghost patterns are found. The spectral resolution varies by  $< 5\%$  for all fibers at a common wavelength due to careful design and alignment of the spectrograph camera. We have made no corrections by convolution to a common resolution. The effect of the spectral resolution variation and the background subtraction scheme is to leave residuals under bright skylines. We characterize the spectral resolution systematic in §3.5. Given the large number of independent spectral elements in VIRUS-P data (126,000 in each dither), we must choose a high significance cut. At  $5\sigma$  significance, the chance of noise leading to a detection at a particular wavelength in a particular dither is only 1 in 14,000. We choose to quote this limit as sufficiently conservative.

### 3.4. Emission line detection

We describe here an automated emission line search algorithm to work with a sky background and continuum subtracted spectrum or stacks of spectra. By applying this search, we robustly find all significant emission lines at all redshifts. In practice, we find no significant  $H\alpha$  emission with plausible velocity offsets in any fiber for either galaxy. Plausible

velocity offsets are determined by the HI rotation curves. In UGC 7321, for example, the rotation curve is flat over our data range with variations of only  $\pm 10 \text{ km s}^{-1}$ . The gas dispersion is measured in the HI data to be near  $7 \text{ km s}^{-1}$  subject to the limitation of the  $5 \text{ km s}^{-1}$  resolution (Uson & Matthews 2003). Over a very conservative  $\pm 100 \text{ km s}^{-1}$  ( $2.2 \text{ \AA}$ ) range around our target wavelengths, the flux limit is flat. First, spectral pixels at any wavelength that exceed the noise by  $1\sigma$  are treated as seeds. Around each seed, we fit Gaussian profiles of variable intensity, width, and central wavelength. The S/N of an emission line is then calculated by summing all pixels and errors in quadrature within  $\pm 2\sigma_{res}$  for the wavelength of interest where  $\sigma_{res}$  is the instrumental dispersion. In the UGC 7321 data,  $\sigma_{res} = 33 \text{ km s}^{-1}$ , and in the UGC 1281 data,  $\sigma_{res} = 100 \text{ km s}^{-1}$ . When quoting limits on undetected emission lines, we sum in quadrature the errors within the same spectral window. These steps in error combination consider both the statistical errors in the reduced data and the systematic error based on ill-matched spectral resolution between fibers discussed in §3.6. A spectral correction factor is divided into the detections and limits to consider the fraction of a Gaussian function's flux that falls outside of the considered window as  $f_{spec} = \text{erf}(\sqrt{2}\sigma_{res}/\sqrt{\sigma_{res}^2 + \sigma_{det}^2})$  where  $\sigma_{det}$  is the detected emission line width. This same factor determines the degradation in flux limit for broad line detections. For unresolved limits,  $\sigma_{det}$  is considered to be zero and the spectral correction ( $f_{spec}^{-1}$ ) evaluates as  $\times 1.05$ . In practice, we make no significant detections within  $\pm 500 \text{ km/s}$  of the HI based expected velocity in either galaxy. The average HI heliocentric velocities of UGC 7321 and UGC 1281 are  $407 \text{ km/s}$  (Uson & Matthews 2003) and  $157 \text{ km/s}$  (García-Ruiz et al. 2002) with the asymptotic HI velocities nearest our pointings at  $\sim 510 \text{ km/s}$  and  $\sim 210 \text{ km/s}$  respectively. We observed under topocentric radial velocities of  $-12 \text{ km/s}$  and  $3 \text{ km/s}$  toward UGC 7321 and UGC 1281 respectively. Therefore, we expect unresolved H $\alpha$  emission at  $6573.7 \pm 0.4 \text{ \AA}$  and  $6567.5 \pm 0.8 \text{ \AA}$  using the asymptotic values just quoted, in the observed frames of UGC 7321 and UGC 1281 respectively. The gas velocity dispersions in the 21 cm data are of the order  $7 \text{ km s}^{-1}$ . The 21 cm rotation curves change by  $\pm 10 \text{ km s}^{-1}$  over our fields. These two values form the expected wavelength range, and the flux limits around these lines are flat to  $\pm 100 \text{ km s}^{-1}$ .

Background galaxies produce the dominant flux in a number of fibers. This is evident where we can measure redshifts through emission lines identifiable as either Lyman- $\alpha$ , [OII] $\lambda 3727$ , H $\beta$ , [OIII] $\lambda 4959$ , or [OIII] $\lambda 5007$ . For most of the background systems with emission lines the redshift is determined by the pattern of multiple emission lines. If the background galaxies have smooth continuum through our wavelength of interest their removal is accomplished in the continuum removal step. However, the possibility of spectral structure in the continuum across the corresponding H $\alpha$  wavelength range leads us to mask those regions. Operationally, we mask a fiber if it displays a  $5\sigma$  significant value in its continuum as estimated across all available wavelengths under inverse variance weighting. It is also possible that weak continuum is coming from objects in the halo of the target galaxies, in which case the desirability of a mask is less certain. We have performed all the emission line searches and limits with and without this masking process and found no detections in either case. The values we present as limits were made with the masks applied.

### 3.5. Data co-addition and limits

We show the derived limits in Table 2. We find no significant emission lines within the vicinity of the galaxies' velocities (defined as within  $\pm 500 \text{ km s}^{-1}$ ) in any individual fiber. We next mask out continuum sources and apply a circular spatial filter as a 2D Gaussian function kernel with FWHM= $10''$ . Again, we find no significant emission. Finally, we stack all fibers for which the model of §2.1 predicts  $\mu > 10^{-19} \text{ erg/s/cm}^2/\square''$ . The choice of the cut in  $\mu$  is not rigorously determined, but judged as sensible from the shape of the surface brightness distribution in Figure 3 which indicates that many dozens of fibers contain predicted surface brightnesses at roughly one-half the peak value. The co-addition of these fibers to one peak fiber will obviously yield an improved S/N. Different choices in the cut will lead to slightly different formal limits, but the fractional effect is small once large stack sizes of several hundred fibers are reached. The models used to select those fibers are those presented in Table 1 with an assumed  $\Gamma = 4 \times 10^{-14} \text{ s}^{-1}$  and  $\beta = 1.8$ . We use the nearly (Figure 1) linear scaling between  $\Gamma$  and  $\mu$  to determine the true value of  $\Gamma$ . The models predict such averages to yield  $1.7 \times 10^{-19} \text{ erg/s/cm}^2/\square''$  for UGC 7321 and  $1.8 \times 10^{-19} \text{ erg/s/cm}^2/\square''$  for UGC 1281. We again find no significant emission in the stacked spectra. These emission line searches were performed solely with errors based on Poisson noise statistics and yielded no detections. In §3.6 we discuss additional systematic errors that degrade the final limits derived from purely Poisson errors in the data. By the models, the peak H $\alpha$  surface brightness would have fallen in our fields for UVB strengths from  $2 \times 10^{-14} \text{ s}^{-1} < \Gamma < 2 \times 10^{-12} \text{ s}^{-1}$  and warps of  $< 12.4^\circ$  in UGC 7321 and  $4 \times 10^{-15} \text{ s}^{-1} < \Gamma < 3 \times 10^{-13} \text{ s}^{-1}$  and warps of  $< 15.8^\circ$  in UGC 1281. However, a radial displacement of the field would still give significant flux as seen in the contour plots, so we do not expect misalignments to affect the final limits. Figure 3 shows the positions of the observations relative to several key features. The 21 cm data contours are overlaid, the locations of masked background galaxies are shown, and the expected spatial profiles of H $\alpha$  emission is shown. We show in Figure 4 the sky spectra and the three types of spectral stacks to background subtracted data in UGC 7321. In Figure 5 we show the corresponding ones for UGC 1281. In neither case do we make a significant detection in H $\alpha$ .

Our selection of fibers for co-addition based on an assumed value of  $\Gamma$  leads us in turn to a lower limit on  $\Gamma$ . This may in principle introduce an error into our determination of  $\Gamma$ . However, both a rough estimation and then a detailed analysis show that the non-linearity in this operation is negligible. First, one measure of the spatial scale of the H $\alpha$  surface brightness profile is the threshold radius,  $r_c$ , of Equation 5. Since  $r_c$  scales only as the natural logarithm of  $\Gamma$ , there is little change over the range of possible UVB strengths that we consider. The shape of the H $\alpha$  surface brightness profile is also broad and smooth, from Figure 3, relative to the possible range of  $r_c$ . By selecting wide swaths of fibers for co-addition, the problem is particularly well behaved. Second, we verify these arguments with a numerical example. We simulated the surface brightness profiles for  $\Gamma = 8 \times 10^{-15} \text{ s}^{-1}$ , or five times lower than the nominal modeled value. We sampled the same set of fibers for co-addition as with the previous analysis. The model, average surface brightness was  $\mu = 3.1 \times 10^{-20} \text{ erg/s/cm}^2/\square''$  and  $\mu = 3.9 \times 10^{-20} \text{ erg/s/cm}^2/\square''$  for UGC 7321 and UGC 1281 respectively, or

only 6% lower and 10% higher than the linear prediction. We conclude that the selection of co-added fibers based on the nominal UVB strength has negligible impact on our final limit.

### 3.6. Error assessment

There are several potential sources of systematic error to the presented spectra. We have already discussed the uncertainties in the model-based conversion of  $H\alpha$  surface brightness to UVB strength in §2.2. The uncertainty in the absolute spectral flux calibration due to the applied atmospheric extinction curve is discussed in §3. The uncertainty in the absolute spectral flux calibration due to the standard star observations is discussed in §3.1. We now analyze a final systematic regarding the relative error determinations in the  $H\alpha$  spectra. We observe that the propagation of the errors from the data's original read noise and shot noise does not fully account for the variation in sky subtracted spectra. This is especially true under bright skylines. We discuss three possible causes with a focus on the variation of spectral resolution across different fibers. In any of the cases, the form of the systematic error will be to add a small percentage of the continuum subtracted sky background spectrum applied linearly with the random error.

First, the instrumental spectral resolution varies by at most 5% in different fibers due to small but detectable optical distortions in the camera. We further measure from arc lamp exposures that the variation is 2.5% between the sky and science fibers in the UGC 7321 data and 1.5% in the UGC 1281 data. These factors are presented in column 3 of Table 2 and scaled by the background subtracted sky spectrum and applied as systematic errors in the spectra presented in Figures 4 and 5. This form of the systematic, as the fractional error in the dispersion times the background subtracted sky spectrum, can be derived simply by taking the first order expansion of a Gaussian function near the line center. Second, the fiber-to-fiber throughput can vary slightly between flat field calibrations. The relative fiber-to-fiber throughput is calibrated with sky flats taken at dawn and dusk. This relative throughput has been measured to be stable to  $<5\%$  over most nights. However, we find a maximum 15% fiber-to-fiber throughput variation in the UGC 7321 data due to poor fiber cable coiling practices. This error is very evident in the broadband estimate per fiber as shown in Figure 3. The error is less important for a continuum subtracted spectral element where most of the fiber-to-fiber throughput error subtracts out. The form of the throughput variation is that a few fibers experience a change with time, but the majority stay stable. We measure the rms throughput variation between all fibers to be far below 1%. Third, sky lines may vary across the  $\sim 1'$  separating the sky and science fibers. The UGC 7321 fiducial “signal” is well resolved from all known sky lines and only near OH lines, but the UGC 1281 “signal” is unresolved from an OH line and near the geocoronal  $H\alpha$ . Variations on such small spatial scales have not been observed, and the data are averaged over very long integration times and large ranges in zenith distance, so we do not expect sky variation over our field-of-view to be a dominant error term. It is possible that the geocoronal  $H\alpha$  emission may vary within  $\sim 1'$ , but small-scale variation is less likely for OH. We choose to parameterize the total effect of these systematics in a conservative manner by deriving from the data themselves the systematic error based on the measured levels of spectral resolution variation seen between fibers.

This systematic error strongly affects the UGC 1281 data since the lower resolution allows blending of night sky lines

at the expected wavelength of  $H\alpha$ , but it is a less important component to the UGC 7321 error budget. As data from more fibers are coadded, this systematic error takes on greater importance in relation to the random error. We assess the  $\chi^2$  distributions across 6300–6600Å in each co-addition case in Table 2. The  $\chi^2$  are simply calculated against a flat, zero flux line and can be visually judged in Figures 4 and 5. The distributions look very symmetric around zero, and the reduced  $\chi^2$  values are consistent with noise. The proper  $\chi^2$  values validate our systematic noise estimates empirically. In fact, the additional noise estimates may be slightly conservative. One can visually note from Figures 4 and 5 that the  $\chi^2$  values are even lower than the degrees of freedom ( $\nu$ ) in the most important regions near the target wavelengths.

### 3.7. Internal galactic extinctions

Internal extinctions in disk galaxies at these scale lengths are very uncertain despite being a subject of detailed research (e.g. Byun *et al.* 1994). Matthews *et al.* (1999) see in UGC 7321 an abrupt truncation of resolved dust clumps beyond  $r \approx 80''$  and fit a model of radially declining dust where, for our position around  $250''$ , there is no internal extinction. We have taken short VIRUS-P exposures covering  $H\alpha$  and  $H\beta$  on the galaxy centers to derive conservative internal extinction upper limit estimates after correction for Galactic extinction. We did not take deep enough exposures to measure accurate stellar populations and photospheric Balmer absorptions ourselves, so we have relied on literature values appropriate to late type galaxies. From the Balmer decrements we measure  $A_{H\alpha} = -0.03 \pm 0.09$  magnitudes for UGC 7321 and  $A_{H\alpha} = -0.02 \pm 0.11$  magnitudes for UGC 1281 under the assumption that the absorption equivalent widths satisfy  $EW(H\alpha)_{abs} = EW(H\beta)_{abs} = 2\text{\AA}$  (McCall *et al.* 1985; Calzetti *et al.* 1994). As the extinction estimates are consistent with zero, we apply no dust correction to our results.

## 4. DISCUSSION

The flux decrement method is currently the most widely used method to estimate the UVB strength at high redshift. Under the fluctuating Gunn-Peterson approximation (Croft *et al.* 1998), the Lyman- $\alpha$  forest optical depth distribution should have a normalization that depends only on well constrained cosmological parameters and the UVB strength. The IGM temperature and density distributions may have some systematic uncertainties that propagate into knowledge of the UVB, but they are not likely the leading uncertainties. The more likely dominant uncertainties in flux decrement modeling are the source emissivities. At  $z \lesssim 1$ , the Lyman limit mean free path becomes larger than the horizon, so the UVB strength at  $z=0$  is influenced by source evolution across this redshift range. AGN and stellar population luminosity functions, both observed and modeled, generally agree to better than an order of magnitude over these redshifts. The least constrained input to flux decrement modeling is the escape fraction for ionizing photons in galaxies, particularly at low redshift and low luminosity. We believe our measurement is best interpreted as an indicator of a low escape fraction.

Our most constraining ( $5\sigma$ ) spectral limits are  $\Gamma < 1.7 \times 10^{-14} \text{ s}^{-1}$  in UGC 7321 and  $\Gamma < 13.5 \times 10^{-14} \text{ s}^{-1}$  in UGC 1281 again assuming  $\beta = 1.8$ . Several benchmarks, both empirical and theoretical, exist with which to compare these limits. Figure 6 shows the UVB strength against redshift



determined by many groups. The lowest redshift proximity effect limit comes from Kulkarni & Fall (1993) with analysis of 13 quasars from Bahcall et al. (1993) between  $0.16 \leq z \leq 1.00$  at  $\Gamma(\bar{z} = 0.5) = 2.0^{+10}_{-1.3} \times 10^{-14} \text{ s}^{-1}$ . However, the proximity effect method has been shown to have a high bias that depends on halo mass (Faucher-Giguère et al. 2008c) and should be interpreted with care. The theoretical model of Faucher-Giguère et al. (2009) gives a drop in the UVB strength by a factor of 3.4 between  $z=0.5$  and  $z=0.0$  leaving this measurement consistent with our current limit. This agreement is interesting and somewhat unexpected given the bias of proximity effect measurements. The only existing low- $z$  flux decrement limit is  $\Gamma(\bar{z} = 0.17) = 5.0^{+20.0}_{-4.0} \times 10^{-14} \text{ s}^{-1}$  (Davé & Tripp 2001). The theoretical model itself, normalized by the flux decrement method, predicts  $\Gamma(z = 0) = 3.8 \times 10^{-14} \text{ s}^{-1}$  which is much higher than our new limit. There exists a second set of unpublished theoretical predictions from F. Haardt and P. Madau discussed in Faucher-Giguère et al. (2009) giving  $\Gamma(z = 0) = 1 \times 10^{-13} \text{ s}^{-1}$ . The latter model used a constant 10% escape fraction of ionizing photons and an unspecified star formation history while the former used a completely theoretical and simulation-based star formation history (Hernquist & Springel 2003) and a scaling of the stellar UV emissivity based on high redshift flux decrement measurements that contains the escape fraction. A comparison to Lyman-break galaxy (LBG) luminosity functions led that group to require only  $f_{esc,abs} \approx 0.5\%$  (Faucher-Giguère et al. 2008b). The direct measurement of galactic escape fractions is difficult due to the low values involved. While UV bright samples can range up to  $\approx 3\%$  in absolute Lyman limit escape fraction (Shapley et al. 2006), a presumably lower-mass sample yielded  $(2 \pm 2)\%$  (Chen et al. 2007). Theoretical work shows a strong decrease in  $f_{esc}$  with star formation rate and halo mass (Gnedin et al. 2008) below  $M_{tot} \approx 10^{11} M_{\odot}$ , and lower redshift observations of populations similar to LBGs show a potential redshift evolution (Siana et al. 2010) with  $f_{esc,abs} < 0.8\%$ . There is no reason yet to suppose a lower bound to the escape fraction. If we interpret our limit as a scaling of the escape fraction from the models in Faucher-Giguère et al. (2008b) at low redshift, we find  $f_{esc,abs} < 0.2\%$ .

It is unlikely that systematics from the model assumptions in our analysis can cause the disagreement. Contaminating ionization from the galaxies' forming stars would bias our measurement high, only making the disagreement more severe. We further note that the degree of contamination can be measured by anomalous [NII] $\lambda$ 6548 to H $\alpha$  ratios (BFQ) and should not, in principle, limit this type of measurement. There has been a large body of work on low strength star formation beyond the optical radii in local galaxy disks, usually labelled extended UV disks (XUV), fostered by far UV (FUV, 1350-1750Å) and near UV (1750-2750Å) Galaxy Evolution Explorer (GALEX) data (e.g. Thilker et al. 2007). Narrowband H $\alpha$  imaging and spectroscopy have revealed that  $\sim 10\%$  of gas rich disks (Werk et al. 2010a,b; Herbert-Fort et al. 2010) host outlying H $\alpha$  emitting complexes as either compact HII regions or dwarf satellite companions. The common H $\alpha$  fluxes observed so far are of the order of a few times  $10^{-16} \text{ erg/s/cm}^2$ . Any such systems would have been found in our

data as strong detections limited in size to a few fibers. The expectation of large-scale, diffuse UVB H $\alpha$  emission should discriminate reliably against compact XUV H $\alpha$  emission. We have also visually inspected the target galaxies' GALEX data which have not yet been analyzed in any XUV focused work. UGC 1281 has only been covered in the rather shallow all-sky survey mode. UGC 7321 has been covered for 2.8ks in the NUV and 1.7 ks in the FUV under guest investigator cycle 4 proposal ID 095 (PI: J. Lee) as part of the 11HUGS project (Lee et al. 2009). In neither system is there evidence for an extended UV disk beyond the DSS2-red<sup>3</sup> limiting contours. Finally, these contamination issues are speculative until a putative UVB H $\alpha$  detection is made. The only possible systematics that could have made a low bias to our limit are unaccounted for dust or gas distribution parameters, such as inclination, far beyond the range we have constrained.

We have made our first analysis under the assumption that the gas distribution extends beyond the HI data limits with the same exponential form as at smaller radii. This assumption, motivated by the thin and regular HI distributions and lack of nearby companions, has the strongest impact on our interpretation. An alternative estimate without this assumption, taking only fibers that overlap with the observed HI signal, yields a very comparable limit of  $\Gamma < 2.3 \times 10^{-14} \text{ s}^{-1}$  at  $5\sigma$  significance in UGC 7321. This agreement essentially comes about because our original model predicts only a minor H $\alpha$  contribution at the discarded positions under the modeled UVB strength. Nevertheless, there is no reason to assume the presence of an HI edge since the radio observations detect the gas up to the column densities where the sensitivity runs out. This result raises the question whether a redshift-dependent escape fraction is manifesting in galaxies. Alternatively, our new limits may be saying that the UVB strength, as estimated through flux decrement measurements, has been overestimated at all redshifts. The latter choice would upset the apparent agreement between current models and reionization constraints. Either case will require some modification to the UVB strength model and its implementation in structure formation simulations. We intend to pursue our measurements of these and other superthin galaxies to greater depth in order to arrive at a detection of  $\Gamma(z = 0)$ .

We thank Karl Gebhardt, Guillermo Blanc, Benjamin Weiner, Jeremy Murphy, and Joss Bland-Hawthorn for fruitful discussion on this topic. The skills of the McDonald Observatory staff, and in particular David Doss, have been indispensable to this project. J.M.U. appreciates the support of a "Bourse de la Ville de Paris" during part of this research. J.J.A. acknowledges the support of a National Science Foundation Graduate Research Fellowship and a UT David Bruton, Jr. Fellowship during this work. This work was partially supported by a Texas Norman Hackerman Advanced Research Program under grant 003658-0295-2007. We thank the Cynthia and George Mitchell Foundation for funding the VIRUS-P instrument. Finally, we thank an anonymous referee for very important improvements to this work. *Facilities:* Smith (VIRUS-P).

## APPENDIX

FULL SOLUTION TO THE GENERAL H $\alpha$  SURFACE BRIGHTNESS

We give here the derivation of the general H $\alpha$  surface brightness at field positions  $b_1$  and  $b_2$ . The special case for  $b_1=r_c$  and  $b_2=0$  was derived as Equation 9. That case is simplified since the line of sight integration can proceed from zero to infinity without intersecting the photoionization boundary and has symmetry between positive and negative values of  $\rho$ . For the general case, the simple task presented in this Appendix is to find the possible geometrical intersections of  $z$  from Equation 7 and  $z_c(R)$  from Equation 6 as a function of  $\rho$  under inputs  $i$ ,  $b_1$ , and  $b_2$ . This may have zero or two intersections labelled as  $\rho_{r1}$  and  $\rho_{r2}$ . Once found, the general expression for  $\mu$  then follows Equation A1.

$$\mu(b_1, b_2) = \frac{\xi^2 \varepsilon \alpha_{H\alpha}^{eff} n_0^2 h \nu_{H\alpha} \gamma}{\Omega}$$

$$\text{with } \gamma = \begin{cases} \int_{-\infty}^{\infty} \exp\left(-\frac{2\rho \cos i}{h_z} - \frac{2\sqrt{r_c^2 + \rho^2 \sin^2 i}}{h_r}\right) d\rho & : \text{no roots in } \rho \\ \int_{-\infty}^{\rho_{r1}} \exp\left(-\frac{2\rho \cos i}{h_z} - \frac{2\sqrt{r_c^2 + \rho^2 \sin^2 i}}{h_r}\right) d\rho + \\ \int_{\rho_{r2}}^{\infty} \exp\left(-\frac{2\rho \cos i}{h_z} - \frac{2\sqrt{r_c^2 + \rho^2 \sin^2 i}}{h_r}\right) d\rho & : \text{roots in } \rho \end{cases} \quad (\text{A1})$$

The first necessary condition for any intersection to occur is evidently expressed in Equation A2, as the largest possible distance for an intersection to lie from the galaxy center is  $r_c$  while the closest possible approach for a sight line is  $b_1$ .

$$b_1 < r_c \quad (\text{A2})$$

The intersections in  $\rho$  can be expanded into simple quadratic equations. Each of the two potential roots from the quadratic solution is double valued when considering intersections with both signs of the  $z_c(R)$  surface leading to four possible roots. However, only at most two of the roots will be physical with the rejected two lying on extrapolations of  $z_c(R)$  at  $R(\rho) > r_c$  or  $|z(\rho)| > r_c \times h_z/h_r$ . The intersections with these surfaces lead to possible limits  $\rho_{s1}$ ,  $\rho_{s2}$ ,  $\rho_{s3}$ , and  $\rho_{s4}$  expressed in Equations A3-A6. The most constraining limits are then the values between these four with the smallest absolute values leading to Equations A7-A8 for the active limits  $\rho_{l1}$  and  $\rho_{l2}$ .

$$\rho_{s1} = \frac{-b_2 \sin i - \frac{h_z}{h_r} r_c}{\cos i} \quad (\text{A3})$$

$$\rho_{s2} = \frac{b_2 \cos i - \sqrt{r_c^2 - b_1^2}}{\sin i} \quad (\text{A4})$$

$$\rho_{s3} = \frac{-b_2 \sin i + \frac{h_z}{h_r} r_c}{\cos i} \quad (\text{A5})$$

$$\rho_{s4} = \frac{b_2 \cos i + \sqrt{r_c^2 - b_1^2}}{\sin i} \quad (\text{A6})$$

$$\rho_{l1} = \max(\rho_{s1}, \rho_{s2}) \quad (\text{A7})$$

$$\rho_{l2} = \min(\rho_{s3}, \rho_{s4}) \quad (\text{A8})$$

The potential intersections with  $z_c(R)$  can be directly evaluated as  $\rho_{p1}$ ,  $\rho_{p2}$ ,  $\rho_{p3}$ , and  $\rho_{p4}$  as given in Equations A9-A12.

$$\rho_{p1} = \frac{\left(\frac{h_r}{h_z}\right) r_c \cos i - \left(\frac{h_r}{h_z}\right)^2 b_2 \sin i \cos i - b_2 \sin i \cos i + \sqrt{\beta_{p1}}}{\left(\frac{h_r}{h_z}\right)^2 \cos^2 i - \sin^2 i}$$

$$\beta_{p1} = 2 \left(\frac{h_r}{h_z}\right)^2 b_2^2 \cos^2 i \sin^2 i - 2 \left(\frac{h_r}{h_z}\right) b_2 r_c \cos^2 i \sin i + b_1^2 \left(\frac{h_r}{h_z}\right)^2 \cos^2 i$$

$$+ b_2^2 \left(\frac{h_r}{h_z}\right)^2 \sin^2 i + r_c^2 \sin^2 i + \left(\frac{h_r}{h_z}\right)^2 b_2^2 \sin^4 i - 2 \left(\frac{h_r}{h_z}\right) r_c b_2 \sin^3 i - b_1^2 \sin^2 i \quad (\text{A9})$$

$$\rho_{p2} = \frac{\left(\frac{h_r}{h_z}\right) r_c \cos i - \left(\frac{h_r}{h_z}\right)^2 b_2 \sin i \cos i - b_2 \sin i \cos i - \sqrt{\beta_{p1}}}{\left(\frac{h_r}{h_z}\right)^2 \cos^2 i - \sin^2 i}$$

$$\beta_{p1} = 2 \left(\frac{h_r}{h_z}\right)^2 b_2^2 \cos^2 i \sin^2 i - 2 \left(\frac{h_r}{h_z}\right) b_2 r_c \cos^2 i \sin i + b_1^2 \left(\frac{h_r}{h_z}\right)^2 \cos^2 i$$

$$+ b_2^2 \left(\frac{h_r}{h_z}\right)^2 \sin^2 i + r_c^2 \sin^2 i + \left(\frac{h_r}{h_z}\right)^2 b_2^2 \sin^4 i - 2 \left(\frac{h_r}{h_z}\right) r_c b_2 \sin^3 i - b_1^2 \sin^2 i \quad (\text{A10})$$

$$\begin{aligned} \rho_{p3} &= -\frac{\left(\frac{h_r}{h_z}\right) r_c \cos i - \left(\frac{h_r}{h_z}\right)^2 b_2 \sin i \cos i - b_2 \sin i \cos i + \sqrt{\beta_{p2}}}{\left(\frac{h_r}{h_z}\right)^2 \cos^2 i - \sin^2 i} \\ \beta_{p2} &= 2 \left(\frac{h_r}{h_z}\right)^2 b_2^2 \cos^2 i \sin^2 i + 2 \left(\frac{h_r}{h_z}\right) b_2 r_c \cos^2 i \sin i + b_1^2 \left(\frac{h_r}{h_z}\right)^2 \cos^2 i \\ &+ b_2^2 \left(\frac{h_r}{h_z}\right)^2 \sin^2 i + r_c^2 \sin^2 i + \left(\frac{h_r}{h_z}\right)^2 b_2^2 \sin^4 i + 2 \left(\frac{h_r}{h_z}\right) r_c b_2 \sin^3 i - b_1^2 \sin^2 i \end{aligned} \quad (\text{A11})$$

$$\begin{aligned} \rho_{p4} &= -\frac{\left(\frac{h_r}{h_z}\right) r_c \cos i - \left(\frac{h_r}{h_z}\right)^2 b_2 \sin i \cos i - b_2 \sin i \cos i - \sqrt{\beta_{p2}}}{\left(\frac{h_r}{h_z}\right)^2 \cos^2 i - \sin^2 i} \\ \beta_{p2} &= 2 \left(\frac{h_r}{h_z}\right)^2 b_2^2 \cos^2 i \sin^2 i + 2 \left(\frac{h_r}{h_z}\right) b_2 r_c \cos^2 i \sin i + b_1^2 \left(\frac{h_r}{h_z}\right)^2 \cos^2 i \\ &+ b_2^2 \left(\frac{h_r}{h_z}\right)^2 \sin^2 i + r_c^2 \sin^2 i + \left(\frac{h_r}{h_z}\right)^2 b_2^2 \sin^4 i + 2 \left(\frac{h_r}{h_z}\right) r_c b_2 \sin^3 i - b_1^2 \sin^2 i \end{aligned} \quad (\text{A12})$$

The comparisons to the limits  $\rho_{l1}$  and  $\rho_{l2}$  discard unphysical values in Equations A13-A14 where the final limits of integration are found.

$$\rho_{r1} = \min(x \in \{\rho_{p1}, \rho_{p2}, \rho_{p3}, \rho_{p4}\} : \rho_{l1} < x < \rho_{l2}) \quad (\text{A13})$$

$$\rho_{r2} = \max(x \in \{\rho_{p1}, \rho_{p2}, \rho_{p3}, \rho_{p4}\} : \rho_{l1} < x < \rho_{l2}) \quad (\text{A14})$$

With the integration boundaries now well defined,  $\mu(b_1, b_2)$  can easily be obtained through numerical integration.

#### REFERENCES

- Adams, J. J., Hill, G. J., & MacQueen, P. J. 2008, in Proc. SPIE, Vol. 7014, 232  
Adams, J. J., et al. 2010, accepted to ApJS, ArXiv:1011.0426  
Bahcall, J. N., Bergeron, J., Boksenberg, A., Hartig, G. F., Jannuzi, B. T., Kirhakos, S., Sargent, W. L. W., Savage, B. D., Schneider, D. P., Turnshek, D. A., Weymann, R. J., & Wolfe, A. M. 1993, ApJS, 87, 1  
Bajtlik, S., Duncan, R. C., & Ostriker, J. P. 1988, ApJ, 327, 570  
Beers, T. C., Flynn, K., & Gebhardt, K. 1990, AJ, 100, 32  
Bland-Hawthorn, J., Freeman, K. C., & Quinn, P. J. 1997, ApJ, 490, 143  
Bochkarev, N. G., & Sunyaev, R. A. 1977, AZh, 54, 957  
Bouwens, R. J., Illingworth, G. D., Franx, M., Chary, R., Meurer, G. R., Conselice, C. J., Ford, H., Giavalisco, M., & van Dokkum, P. 2009, ApJ, 705, 936  
Byun, Y. I., Freeman, K. C., & Kylafis, N. D. 1994, ApJ, 432, 114  
Calzetti, D., Kinney, A. L., & Storchi-Bergmann, T. 1994, ApJ, 429, 582  
Carignan, C., & Purton, C. 1998, ApJ, 506, 125  
Carswell, R. F., Whelan, J. A. J., Smith, M. G., Boksenberg, A., & Tytler, D. 1982, MNRAS, 198, 91  
Cen, R., Miralda-Escudé, J., Ostriker, J. P., & Rauch, M. 1994, ApJ, 437, L9  
Chen, H., Prochaska, J. X., & Gnedin, N. Y. 2007, ApJ, 667, L125  
Christlein, D., & Zaritsky, D. 2008, ApJ, 680, 1053  
Christlein, D., Zaritsky, D., & Bland-Hawthorn, J. 2010, MNRAS, 641  
Corbelli, E., Schneider, S. E., & Salpeter, E. E. 1989, AJ, 97, 390  
Croft, R. A. C., Weinberg, D. H., Katz, N., & Hernquist, L. 1998, ApJ, 495, 44  
Davé, R., & Tripp, T. M. 2001, ApJ, 553, 528  
Dierckx, P. 1993, Curve and surface fitting with splines (Monographs on Numerical Analysis, Oxford: Clarendon, —c1993)  
Donahue, M., Aldering, G., & Stocke, J. T. 1995, ApJ, 450, L45+  
Dove, J. B., & Shull, J. M. 1994, ApJ, 423, 196  
Efstathiou, G. 1992, MNRAS, 256, 43P  
Fardal, M. A., Giroux, M. L., & Shull, J. M. 1998, AJ, 115, 2206  
Faucher-Giguère, C., Lidz, A., Hernquist, L., & Zaldarriaga, M. 2008a, ApJ, 682, L9  
—, 2008b, ApJ, 688, 85  
Faucher-Giguère, C., Lidz, A., Zaldarriaga, M., & Hernquist, L. 2008c, ApJ, 673, 39  
—, 2009, ApJ, 703, 1416  
Felten, J. E., & Bergeron, J. 1969, Astrophys. Lett., 4, 155  
Gallego, J., Zamorano, J., Aragon-Salamanca, A., & Rego, M. 1995, ApJ, 455, L1+  
García-Ruiz, I., Sancisi, R., & Kuijken, K. 2002, A&A, 394, 769  
Gnedin, N. Y., Kravtsov, A. V., & Chen, H. 2008, ApJ, 672, 765  
Haardt, F., & Madau, P. 1996, ApJ, 461, 20  
Herbert-Fort, S., Zaritsky, D., Christlein, D., & Kannappan, S. J. 2010, ApJ, 715, 902  
Hernquist, L., & Springel, V. 2003, MNRAS, 341, 1253  
Hill, G. J., et al. 2008, in Proc. SPIE, Vol. 7014, 231  
Hopkins, A. M. 2004, ApJ, 615, 209

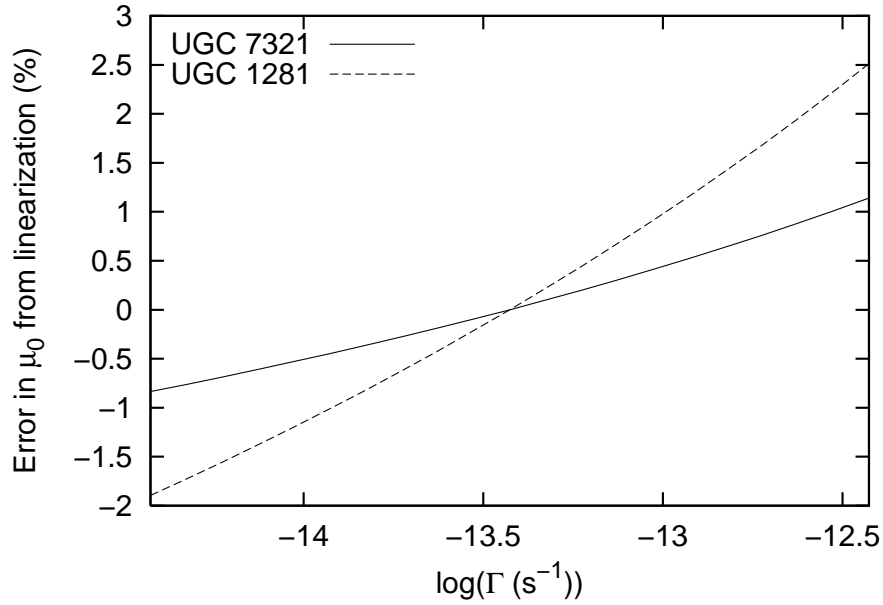


**Figure 1.** The fractional error in a linear relation between the H $\alpha$  peak surface brightness and the UVB photoionization rate,  $\Gamma$ , under different UVB strengths. The parameters for the two target galaxies are given in Table 1 and their derivation described in §2.2. The pivot in the linearization at  $\Gamma = 4 \times 10^{-14} \text{ s}^{-1}$  represents the current best estimate from Faucher-Giguère *et al.* (2009).

- Hopkins, P. F., Richards, G. T., & Hernquist, L. 2007, *ApJ*, 654, 731  
Huchtmeier, R. 1989, *A General Catalog of HI Observations of Galaxies. The Reference Catalog.*, ed. Huchtmeier, W. K., Richter, O.-G.  
Hui, L., & Gnedin, N. Y. 1997, *MNRAS*, 292, 27  
Kelson, D. D. 2003, *PASP*, 115, 688  
Kennicutt, Jr., R. C. 1989, *ApJ*, 344, 685  
Kulkarni, V. P., & Fall, S. M. 1993, *ApJ*, 413, L63  
Lee, J. C., Gil de Paz, A., Tremonti, C., Kennicutt, R. C., Salim, S., Bothwell, M., Calzetti, D., Dalcanton, J., Dale, D., Engelbracht, C., Funes, S. J. J. G., Johnson, B., Sakai, S., Skillman, E., van Zee, L., Walter, F., & Weisz, D. 2009, *ApJ*, 706, 599  
Loeb, A., & Eisenstein, D. J. 1995, *ApJ*, 448, 17  
Madau, P., Haardt, F., & Rees, M. J. 1999, *ApJ*, 514, 648  
Madsen, G. J., Reynolds, R. J., Haffner, L. M., Tufte, S. L., & Maloney, P. R. 2001, *ApJ*, 560, L135  
Maloney, P. 1993, *ApJ*, 414, 41  
Massey, P., Strobel, K., Barnes, J. V., & Anderson, E. 1988, *ApJ*, 328, 315  
Matthews, L. D., Gallagher, III, J. S., & van Driel, W. 1999, *AJ*, 118, 2751  
McCall, M. L., Rybski, P. M., & Shields, G. A. 1985, *ApJS*, 57, 1  
O'Donnell, J. E. 1994, *ApJ*, 422, 158  
Oosterloo, T., Fraternali, F., & Sancisi, R. 2007, *AJ*, 134, 1019  
Osterbrock, D. E., & Ferland, G. J. 2006, *Astrophysics of gaseous nebulae and active galactic nuclei*  
Rauch, M., Haehnelt, M. G., & Steinmetz, M. 1997a, *ApJ*, 481, 601  
Rauch, M., Miralda-Escude, J., Sargent, W. L. W., Barlow, T. A., Weinberg, D. H., Hernquist, L., Katz, N., Cen, R., & Ostriker, J. P. 1997b, *ApJ*, 489, 7  
Schirber, M., & Bullock, J. S. 2003, *ApJ*, 584, 110  
Schlegel, D. J., Finkbeiner, D. P., & Davis, M. 1998, *ApJ*, 500, 525  
Shapley, A. E., Steidel, C. C., Pettini, M., Adelberger, K. L., & Erb, D. K. 2006, *ApJ*, 651, 688  
Shull, J. M., Roberts, D., Giroux, M. L., Penton, S. V., & Fardal, M. A. 1999, *AJ*, 118, 1450  
Siana, B., Teplitz, H. I., Ferguson, H. C., Brown, T. M., Giavalisco, M., Dickinson, M., Chary, R., de Mello, D. F., Conselice, C. J., Bridge, C. R., Gardner, J. P., Colbert, J. W., & Scarlata, C. 2010, *ArXiv e-prints*  
Stoche, J. T., Case, J., Donahue, M., Shull, J. M., & Snow, T. P. 1991, *ApJ*, 374, 72  
Sunyaev, R. A. 1969, *Astrophys. Lett.*, 3, 33  
Thilker, D. A., Bianchi, L., Meurer, G., Gil de Paz, A., Boissier, S., Madore, B. F., Boselli, A., Ferguson, A. M. N., Muñoz-Mateos, J. C., Madsen, G. J., Hameed, S., Overzier, R. A., Forster, K., Friedman, P. G., Martin, D. C., Morrissey, P., Neff, S. G., Schiminovich, D., Seibert, M., Small, T., Wyder, T. K., Donas, J., Heckman, T. M., Lee, Y., Milliard, B., Rich, R. M., Szalay, A. S., Welsh, B. Y., & Yi, S. K. 2007, *ApJS*, 173, 538  
Tully, R. B., Rizzi, L., Dolphin, A. E., Karachentsev, I. D., Karachentseva, V. E., Makarov, D. I., Makarova, L., Sakai, S., & Shaya, E. J. 2006, *AJ*, 132, 729  
Uson, J. M., & Matthews, L. D. 2003, *AJ*, 125, 2455  
van Gorkom, J. 1993, in *Astrophysics and Space Science Library*, Vol. 188, *The Environment and Evolution of Galaxies*, ed. J. M. Shull & H. A. Thronson, 345–  
Vogel, S. N., Weymann, R., Rauch, M., & Hamilton, T. 1995, *ApJ*, 441, 162  
Walsh, W., Staveley-Smith, L., & Oosterloo, T. 1997, *AJ*, 113, 1591  
Werk, J. K., Putman, M. E., Meurer, G. R., Ryan-Weber, E. V., Kehrig, C., Thilker, D. A., Bland-Hawthorn, J., Drinkwater, M. J., Kennicutt, R. C., Wong, O. I., Freeman, K. C., Oey, M. S., Dopita, M. A., Doyle, M. T., Ferguson, H. C., Hanish, D. J., Heckman, T. M., Kilborn, V. A., Kim, J. H., Knezek, P. M., Koribalski, B., Meyer, M., Smith, R. C., & Zwaan, M. A. 2010a, *AJ*, 139, 279  
Werk, J. K., Putman, M. E., Meurer, G. R., Thilker, D. A., Allen, R. J., Bland-Hawthorn, J., Kravtsov, A., & Freeman, K. 2010b, *ApJ*, 715, 656  
Weymann, R. J., Vogel, S. N., Veilleux, S., & Epps, H. W. 2001, *ApJ*, 561, 559

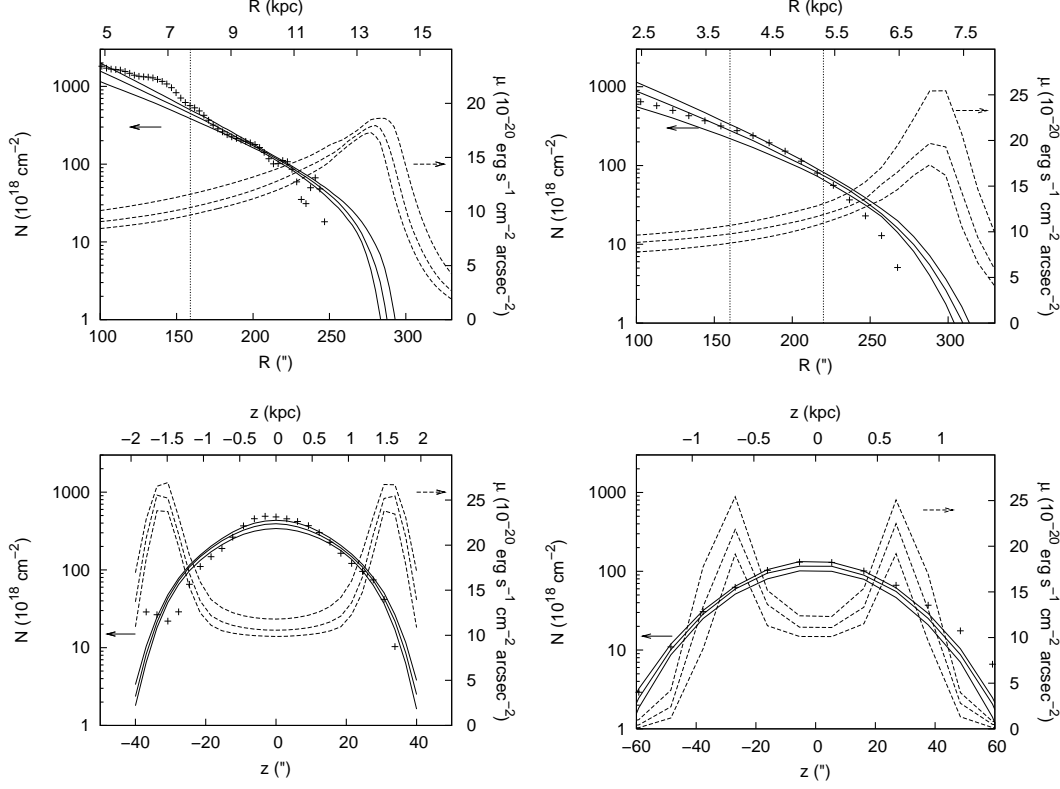


**Figure 2.** The single position angle, parameterized fits to the HI distributions shown as solid lines. Because we assumed a single position angle and single radial scale length, the ranges over which we fit the HI distributions must be somewhat controlled and limited to the radii near the H $\alpha$  observations. The predicted H $\alpha$  surface brightness profiles are also shown against the right side axis as dotted lines. The horizontal arrows indicate the correct axis for each profile. The breaks at large radii in the 21 cm profiles are due to intersections with the UVB photoionization fronts. *Top* The data along the major axes. *Bottom* The data along the minor axes at particular offsets. *Left* Cuts along the midplane and normal to it offset by 165'' with data, models, and 68% confidence intervals in UGC 7321. We restrict the fit to points  $> 160''$  from the galaxy's center as indicated by the vertical dotted line. Using the best parameters from Table 1, the threshold radius (Equation 5) with the nominal value of  $\Gamma = 4 \times 10^{-14} \text{ s}^{-1}$  is predicted to be at  $r_c = 13.4 \text{ kpc}$ . Our spectroscopic data cover regions from  $R = 9.5 \text{ kpc}$  to  $R = 14.6 \text{ kpc}$ . *Right* Similarly, data and fits to UGC 1281. The offset here is 200'' from the minor axis. The points between the dotted lines at 160'' and 220'' form the restricted range of the fit as a  $\approx 8^\circ$  warp becomes important beyond. This fit appears poorer because of the larger warp, but a fit to all points at  $R > 220''$  returns the same radial scale length to within the Monte Carlo errors. Using the best parameters from Table 1, the threshold radius (Equation 5) is predicted to be at  $r_c = 7.4 \text{ kpc}$ . Our spectroscopic data cover regions from  $R = 5.7 \text{ kpc}$  to  $R = 9.1 \text{ kpc}$ . Since we only show one dimensional cuts, these figures do not show all the datapoints used in the fits.

**Table 1**  
HI based model parameters and H $\alpha$  surface brightness predictions\*

Galaxy	$n_0$ ( $\text{cm}^{-3}$ )	$h_z$ (pc)	$h_r$ (kpc)	$i$ ( $^\circ$ )	PA ( $^\circ$ )	$\mu_0$ †	$(\mu \otimes S)_0$ ‡	$\bar{\mu}$ ††	$\mu_{\text{HI}}^{**}$
UGC 7321	$3.3^{+3.5}_{-1.7}$	$426.^{+120.}_{-88.} d_{10}$	$2.12^{+0.25}_{-0.16} d_{10}$	$82.8^{+0.9}_{-0.6}$	$-100.1 \pm 0.1$	$18.4^{+1.0}_{-0.9}$	$16.7^{+1.1}_{-0.7}$	$16.6^{+1.0}_{-0.3}$	$22.5^{+4.3}_{-1.8}$
UGC 1281	$3.8^{+3.2}_{-2.6}$	$303.^{+70.}_{-58.} d_5$	$1.17^{+0.19}_{-0.14} d_5$	$84.9^{+4.0}_{-1.3}$	$-141.3 \pm 0.3$	$21.4^{+12.1}_{-2.8}$	$19.4^{+5.6}_{-2.4}$	$17.9^{+1.7}_{-1.1}$	$13.4^{+6.1}_{-2.0}$

\* Fit under the restricted radial ranges shown in Figure 2 assuming  $\Gamma = 4 \times 10^{-14} \text{ s}^{-1}$  and  $\beta = 1.8$ .

†  $10^{-20} \text{ erg/s/cm}^2/\square''$

‡  $10^{-20} \text{ erg/s/cm}^2/\square''$ , smoothed by a circular 10'' FWHM kernel

††  $10^{-20} \text{ erg/s/cm}^2/\square''$ , average for all fiber positions with predicted values of  $\mu > 10^{-19} \text{ erg/s/cm}^2/\square''$

\*\*  $10^{-20} \text{ erg/s/cm}^2/\square''$ , based on the HI bounded area (Equations 6-8 of Weymann et al. (2001))

**Table 2**  
Error budget and limits to the UVB strength

Co-addition type (1)	Poisson error (2)	Resolution systematic (3)	Flux calibration (4,%)	SB upper limit (5)	Model systematic (6,%)	$\Gamma(z=0)$ upper limit (7)	$\chi^2/\nu$ (8)
UGC 7321 each single fiber	11.0	0.8	8.9	64	+5.4/-4.9	15	353/468
UGC 7321 smoothed	2.8	0.4	8.9	17	+6.6/-4.2	4.4	257/454
UGC 7321 radio bound stack	1.8	0.4	8.9	12	+19.3/-7.9	2.3	545/462
UGC 7321 full stack	0.9	0.4	8.9	7.1	+6.0/-1.8	1.7	497/454
UGC 1281 each single fiber	18.6	29.5	4.3	250	+57/-13	53	68/136
UGC 1281 smoothed	6.6	8.9	4.3	81	+29/-12	19	218/136
UGC 1281 radio bound stack	6.0	8.9	4.3	78	+46/-15	27	261/134
UGC 1281 full stack	2.0	8.9	4.3	57	+9.5/-6.1	14	50/134

(1) Detection and model method. Smoothed refers to a  $10''$  FWHM Gaussian, circular kernel.

(2)  $1\sigma$  ( $10^{-20}$  erg/s/cm<sup>2</sup>/□'') in the spectral data from Poisson noise.

(3)  $1\sigma$  ( $10^{-20}$  erg/s/cm<sup>2</sup>/□'') in the spectral data from spectral resolution or sky line variation. See §3.6.

(4)  $1\sigma$  (%) flux calibration systematic including 2.1% for airmass/extinction error.

(5)  $5\sigma$  ( $10^{-20}$  erg/s/cm<sup>2</sup>/□'') limit in surface brightness. No detections of significance were found, so this limit results simply from summing columns 2 and 3, multiply by one plus the percentage in column 4, and finally multiplying by five.

(6)  $1\sigma$  (%) model surface brightness systematic. These values are derived from the Monte Carlo tests of §2.2.

(7)  $5\sigma$  ( $10^{-14}$  s<sup>-1</sup>) total limit assuming  $\beta = 1.8$ . The achieved H $\alpha$  surface brightness limit is compared to the low bound of the modeled H $\alpha$  surface brightness to create this final, linearized estimate from the modeled value of  $\Gamma = 4 \times 10^{-14}$  s<sup>-1</sup>. This limit results simply by multiplying column 5 by one plus the percentage in column 6, multiplying by the baseline  $\Gamma = 4 \times 10^{-14}$  s<sup>-1</sup> value, and dividing by the lower bound to either column 7, 8, 9, or 10 in Table 1 depending on the limit type.

(8)  $\chi^2$  of all pixels between 6300-6600Å in the spectrum and the degrees of freedom.

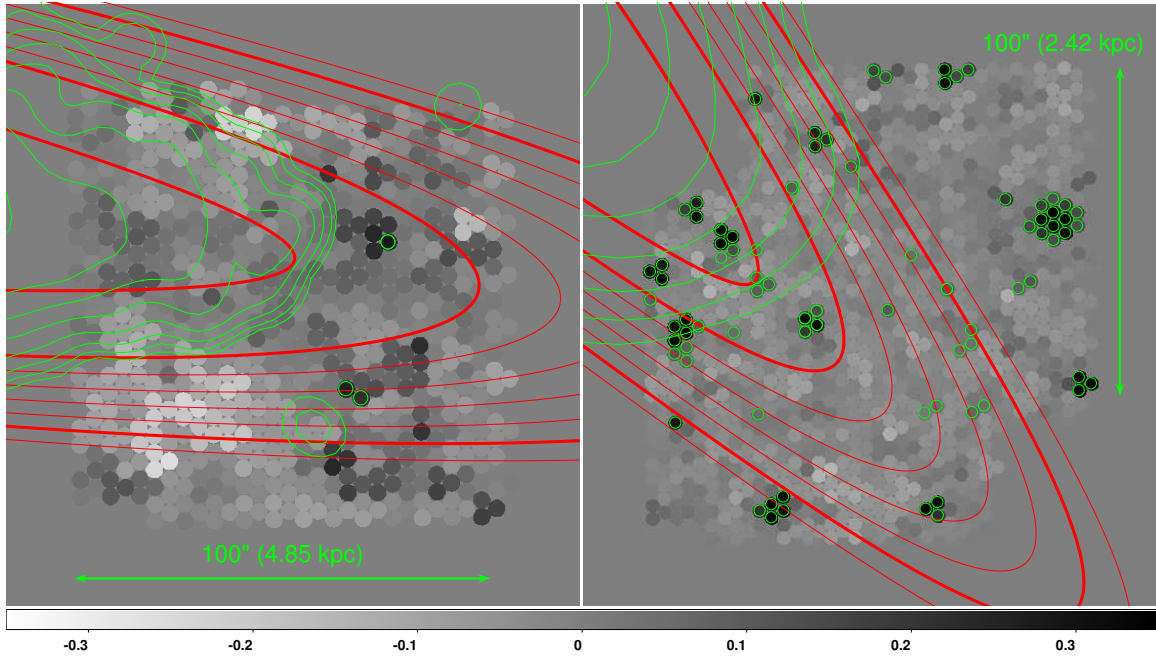


**Figure 3.** *Left* Reconstructed VIRUS-P continuum image of the UGC 7321 outskirts centered at  $\alpha_{J2000}=12:17:16.4$  and  $\delta_{J2000}=+22:31:33$  or  $\approx 250''$  off the minor axis. The continuum estimation is made through the entire available spectral range from 6040-6740Å with the colorbar in units of  $10^{-17}$  erg s<sup>-1</sup> cm<sup>-2</sup> Å<sup>-1</sup>. The dark, circled objects are masked as background galaxies, many known to be background by their emission lines at redshifts higher than the target galaxy's redshift. One can see some broad structure in the continuum map due to small residuals in the fiber-to-fiber throughput as described in §3.6, especially in the UGC 7321 data. The green contours trace the HI column densities in steps of (10,19,36,67,126,238,448,845)  $\times 10^{18}$  cm<sup>-2</sup>. The red, more extended contours trace the predicted H $\alpha$  surface brightness assuming  $\Gamma = 4 \times 10^{-14}$  s<sup>-1</sup> and  $\beta = 1.8$  in contour levels of (0.1,0.24,0.57,1.4,3.3,7.9,19)  $\times 10^{-20}$  erg/s/cm<sup>2</sup>/□''. The two innermost red contours enclose the surface brightness maxima. Positions closer to the center again become dimmer in H $\alpha$  since portions of the gas, in projection, stay neutral at smaller radii. The fibers used in sky subtraction are all those outside the second outermost red contour. We draw the second, seventh, and eighth contours thickly to highlight these regions. As a scale reference, the fiber diameter is  $4''$ . *Right* The same display for UGC 1281 with central position  $\alpha_{J2000}=1:49:15.8$  and  $\delta_{J2000}=+32:31:46$  or  $\approx 300''$  off the minor axis. The continuum estimation is made through the entire available spectral range from 4700-6990Å. Here, many more background galaxies are found. In UGC 1281, we took data at two overlapping fields. The central positions covered by both square pointings have the best depth.

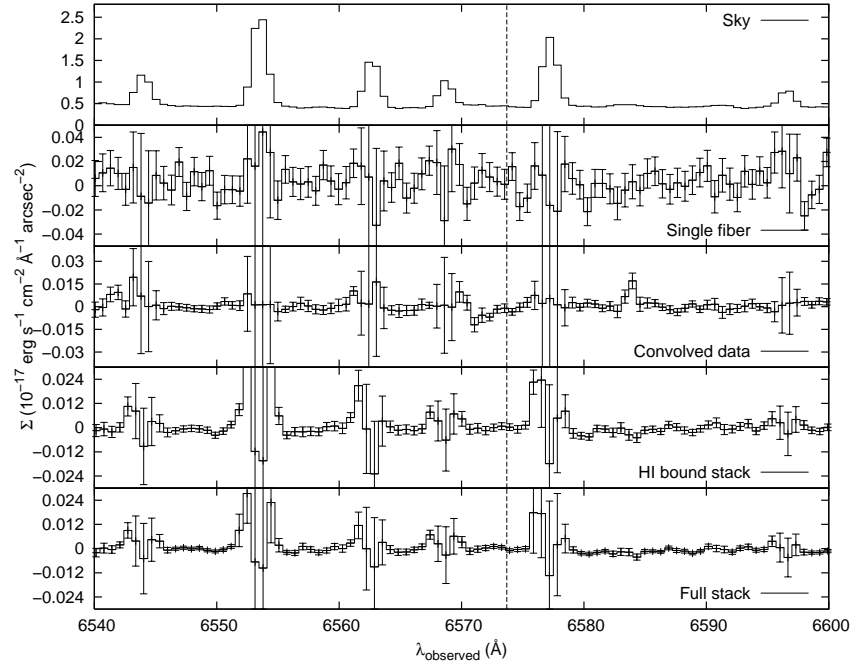


**Figure 4.** Selected spectra around H $\alpha$  in UGC 7321 presented in units of surface brightness. The expected wavelength for emission is shown with a dotted line. The frames from top to bottom show the background sky, the background subtracted spectrum for a typical fiber that does not display continuum, the spectrum at the same position after being smoothed by a  $10''$  FWHM circular Gaussian kernel, the data bounded by HI signal, and finally the stack of the 358 fibers predicted to be the brightest by the model. The errorbars consist of the Poisson, observational error and the systematic spectral resolution error of columns two and three in Table 2 only. The spectral resolution systematic, discussed in §3.6, is most important under the bright skylines and does not dominate at the target wavelength.

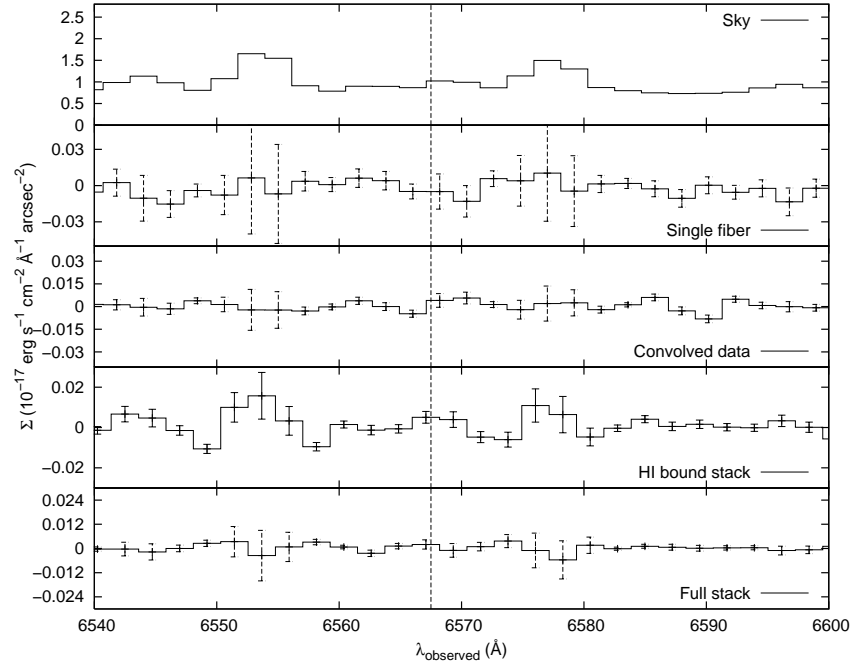


**Figure 5.** Selected surface brightness spectra around H $\alpha$  in UGC 1281. The format is the same as in Figure 4. In this case, 313 of the brightest expected fibers form the final stack.

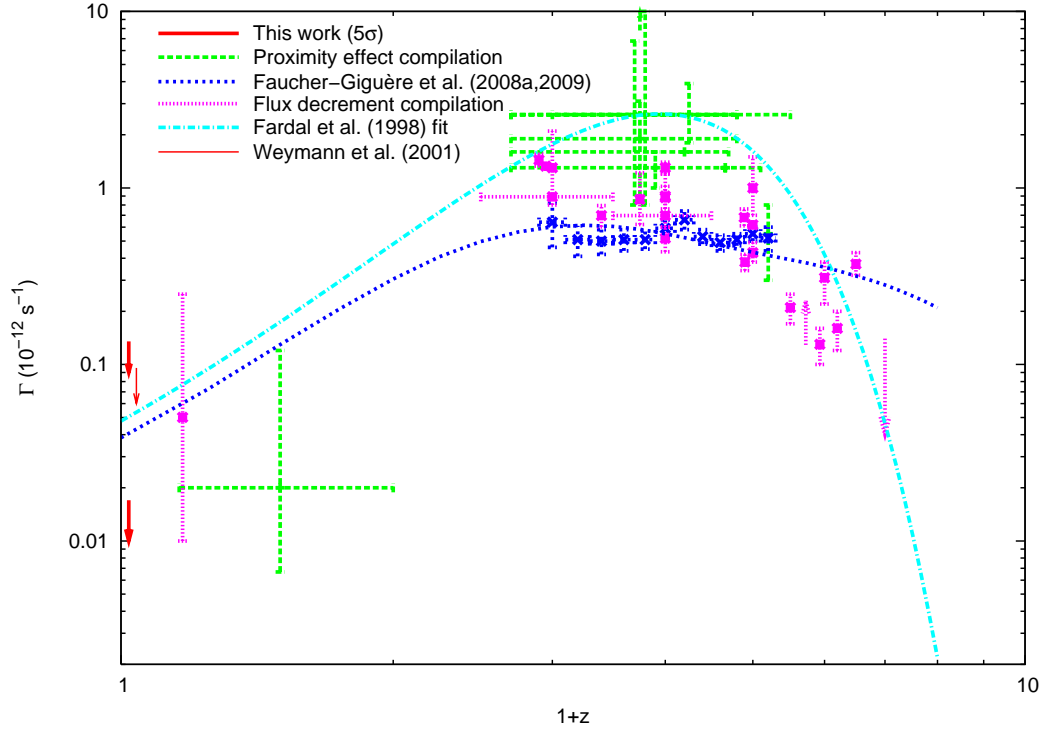


**Figure 6.** A compilation of photoionization rates across redshift. Most of the literature compilations come from Table 2 in Faucher-Giguère et al. (2008c) and Table 1 in Faucher-Giguère et al. (2008b). The flux decrement measurement at  $z \sim 0.17$  is from Davé & Tripp (2001). The low redshift,  $H\alpha$  limit from Weymann et al. (2001) ( $2\sigma$ ) has been the deepest  $z=0$  limit before this work. The UVB fitting function comes from Fardal et al. (1998) and the newer simulation from Faucher-Giguère et al. (2009). Our work's new limit is well below the flux decrement normalized simulation and challenges one or more of the model assumptions. Some points have been slightly shifted in redshift for visual clarity.